Cesium and Laser calibration of the ATLAS Tile Calorimeter

Pratyush Anand[1, a)] and Arely Cortes Gonzalez (Supervisor)[2, b)]

[1)]*Physics Department, Indian Institute of Technology Madras*
[2)]*ATLAS TileCal Group, CERN*

(Dated: 3 August 2018)

The Tile Calorimeter is the hadron calorimeter covering the central region of the ATLAS experiment at the Large Hadron Collider. Approximately 10000 photomultipliers collect light from scintillating tiles acting as the active material between slabs of steel absorber. This paper gives an overview of energy calibration methods. Also the response measurements by the laser and cesium calibration systems of the ATLAS Tile Calorimeter in 2015 are discussed. The study includes:

- Measuring the response drift and the variation of its standard deviation over time.

- Studying the difference between the measurements of two photomultipliers (PMTs) connected to a cell, and its variation over time.

- Comparing the laser and cesium measurement to evaluate a systematic uncertainty for the laser system.

The only calibration that counts is how much heart people invest, how much they ignore their fears of being hurt or caught out or humiliated. And the only thing people regret is that they didn't live boldly enough, that they didn't invest enough heart, didn't love enough. Nothing else really counts at all.
- *Ted Hughes*

---

1. The ATLAS Tile Calorimeter

1.1. Introduction:

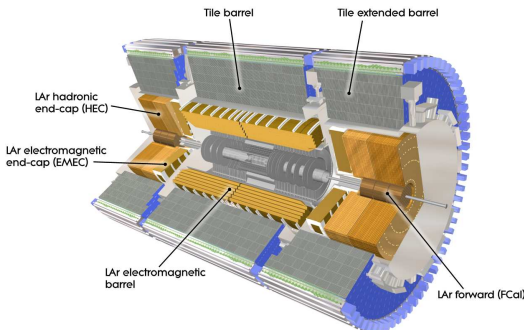The Tile Calorimeter (TileCal) forms the hadronic barrel calorimeter system of the ATLAS detector, which provides essential input to the measurement of the jet energies and to the reconstruction of the missing transverse momentum. The TileCal which surrounds the barrel electromagnetic calorimeter, consists of tiles of plastic scintillator regularly spaced between low-carbon steel absorber plates. The typical thickness in one period are 3mm of the scintillator and 14mm of the absorber parallel to the colliding beams' axis. The calorimeter is divided into three longitudinal segments; one central long barrel (LB) section with 5.8m in length ($|\eta|$ <1.0), and two extended barrel (EB) sections (0.8 <$|\eta|$ <1.7) on either side of the barrel, each 2.6m long.[1] Full azimuthal coverage around the beam axis is achieved with 64 wedge-shaped modules, each covering $\Delta\phi = 0.1$ radians. The TileCal is located at an inner radial distance of 2.28m from the LHC beam-line, and has three radial layers with depths of 1.5, 4.1 and 1.8λ (λ stands for the nuclear interaction length) for the LB, and 1.5, 2.6 and 3.3λ for the EB.

The TileCal design is driven by its ability to reconstruct hadronic jets and missing transverse momentum within the physics programme intended for the ATLAS experiment. For precision measurements involving the reconstruction of jets, the TileCal is designed to have a stand-alone energy resolution for jets of σ/E=50%/$\sqrt{E(GeV)}\oplus$3%. To be sensitive to the full range of energies expected in the LHC lifetime, the response is expected to be linear within 2% for jets up to 4 TeV. Good energy resolution and calorimeter coverage are essential for precise missing transverse momentum reconstruction. A special Intermediate Tile Calorimeter (ITC) system is installed between the LB and EB to correct for energy losses in the region between the two calorimeters.

FIG. 1.1: Part of the ATLAS detector system

[a)]Electronic mail: panand2257@gmail.com
[b)]Electronic mail: arely.cortes.gonzalez@cern.ch
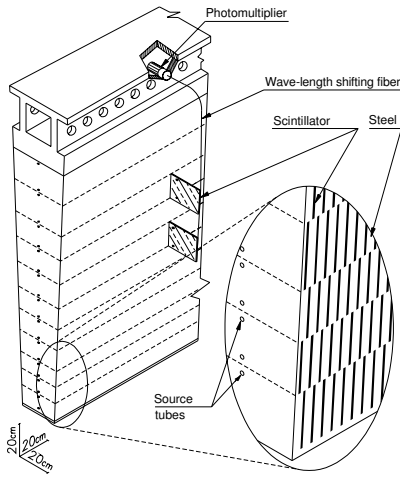
FIG. 1.2: A module of TileCal

FIG. 1.3: Rows and Cells of TileCal

1.2. Structure and read-out electronics:

The light generated in each plastic scintillator is collected at two edges, and then transported to photomultiplier tubes (PMTs) by wavelength shifting (WLS) fibres. The read-out cell geometry is defined by grouping the fibres from individual tiles on the corresponding PMT. A typical cell is read out on each side (edge) by one PMT, each corresponding to one channel. The dimensions of the cells are $\Delta\eta$ x $\Delta\phi$= 0.1 x 0.1 in the first two radial layers, called layers A and BC (just layer B in the EB), and $\Delta\eta$ x $\Delta\phi$= 0.2 x 0.1 in the third layer, referred to as layer D. The projective layout of cells and naming convention are shown in Figure 1.3. The so-called ITC cells (D4, C10 and E-cells) are located between the LB and EB, and provide coverage in the range $0.8 <|\eta| <1.6$. Some of the C10 and D4 cells have reduced thickness or special geometry in order to accommodate services and read-out electronics for other ATLAS detector systems. The gap (E1–E2) and crack (E3–E4) cells are only composed of scintillator and are exceptionally read out by only one PMT. For Run 1, eight crack scintillators were removed per side, to allow for routing of fibres for 16 Minimum Bias Trigger Scintillators (MBTS), used to trigger on events from colliding particles, as well as to free up the necessary electronics channel for read-out of the MBTS. The MBTS scintillators are also read out by the TileCal EB electronics.

The PMTs and front-end electronics are housed in a steel girder at the outer radius of each module in 1.4 m long aluminium units that can be fully extracted while leaving the remaining module in place, and hence are given the name of electronics drawers. Each drawer holds a maximum of 24 channels, two of which form a super-drawer. There are nominally 45 and 32 active channels per super-drawer in the LB and EB, respectively. Each channel consists of a unit called a PMT block, which contains the light-mixer, PMT tube and voltage divider, and
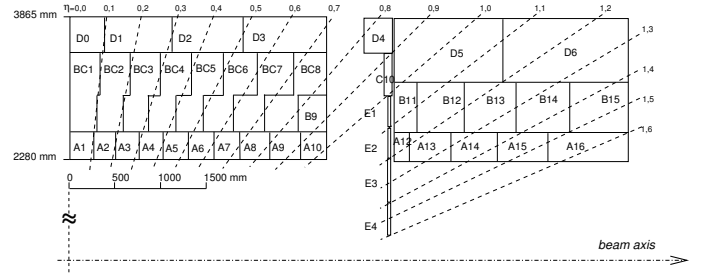
a so-called 3-in-1 card. This card is responsible for fast signal shaping in two gains (with a bi-gain ratio of 1:64), the slow integration of the PMT signal, and provides an input for a charge injection calibration system.

The maximum height of the analogue pulse in a channel is proportional to the amount of energy deposited by the incident particle in the corresponding cell. The shaped signals are sampled and digitised every 25 ns by 10-bit ADCs. The sampled data are temporarily stored in a pipeline memory until a trigger Level-1 signal is received. Seven samples, centred around the pulse peak, are obtained. A gain switch is used to determine which gain information is sent to the back-end electronics for event processing. By default the high-gain signal is used, unless any of the seven samples saturates the ADC, at which point the low-gain signal is transmitted.

Adder boards receive the analogue low-gain signal from the 3-in-1 cards and sum the signal from six 3-in-1 cards within $\Delta\eta \times \Delta\phi = 0.1 \times 0.1$ before transmitting it to the ATLAS hardware-based trigger system as a trigger tower. The integrator circuit measures PMT currents (0.01 nA to 1.4 A) over a long time window of 10–20 ms, and is used for calibration with a radioactive cesium source and to measure the rate of soft interactions during collisions at the LHC. It is a low-pass DC amplifier that receives less than 1% of the PMT current, which is then digitised by a 12-bit ADC card (which saturates at 5 V).

Power is supplied to the front-end electronics of a single super-drawer by means of a low-voltage power supply (LVPS) source, which is positioned in an external steel box mounted just outside the electronics super-drawer. The high voltage is set and distributed to each individual PMT using dedicated boards positioned inside the super-drawers located with the front-end electronics.

The back-end electronics is located in a counting room approximately 100m away from the ATLAS detector. The data acquisition system of the Tile Calorimeter is split into four partitions, the ATLAS A-side ($\eta >0$) and C-side ($\eta <0$) for both the LB and EB, yielding four logical partitions: LBA, LBC, EBA, and EBC. Optical fibres transmit signals between each super-drawer and the back-end trigger, timing and control (TTC) and read-out driver (ROD) crates. There are a total of four TTC and ROD crates, one for each physical partition. The ATLAS TTC system distributes the LHC clock, trigger decisions,

and configuration commands to the front-end electronics. If the TTC system sends the trigger acceptance command to the front-end electronics, the corresponding digital signals for all channels of the calorimeter are sent to the ROD via optical links, where the signal is reconstructed for each channel.

2. Calibration Systems:

Three calibration systems are used to maintain a time-independent electromagnetic (EM) energy scale[2] in the TileCal, and account for changes in the hardware and electronics due to irradiation, ageing, and faults.

- **Cesium (Cs) system** calibrates the scintillator cells and PMTs but not the front-end electronics used for collision data.

- **Laser calibration system** monitors both the PMT and the same front-end electronics used for physics.

- **Charge injection system (CIS)** calibrates and monitors the front- end electronics.

Figure 2.2 shows a flow diagram that summarises the components of the read-out tested by the different calibration systems. These three complementary calibration systems also aid in identifying the source of problematic channels. Problems originating strictly in the read-out electronics are seen by both laser and CIS, while problems related solely to the PMT are not detected by the charge injection system.

The signal amplitude A is reconstructed in units of ADC counts using the OF (Optimal Filtering) algorithm. The conversion to channel energy, $E_{channel}$, is performed with the following formula:

$$E_{channel} = A \times C_{Cs} \times C_{laser} \times C_{ADC \to pC,CIS}/C_{TB} \quad (1)$$

where each C_i represents a calibration constant or correction factor, which are described in the following paragraphs.

The overall EM scale C_{TB} was determined in dedicated beam tests with electrons incident on 11% of the production modules. It amounts to 1.050 ± 0.003 pC/GeV with an RMS spread of $(2.4 \pm 0.1)\%$ in layer A, with
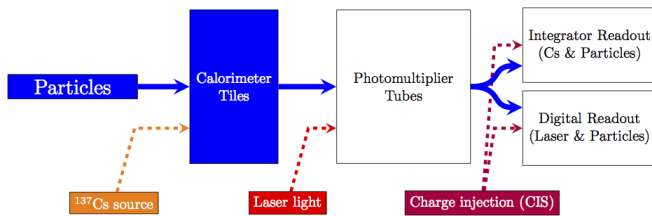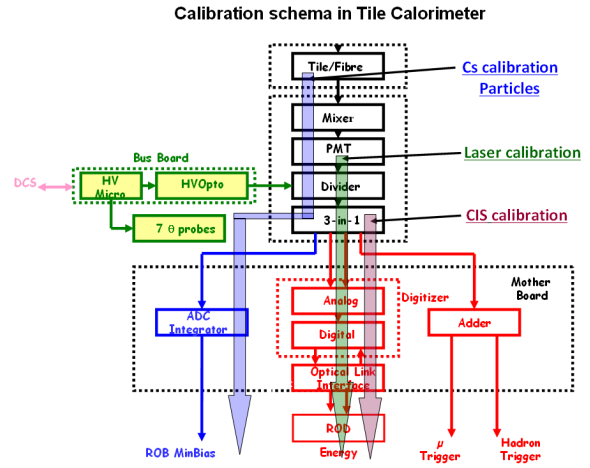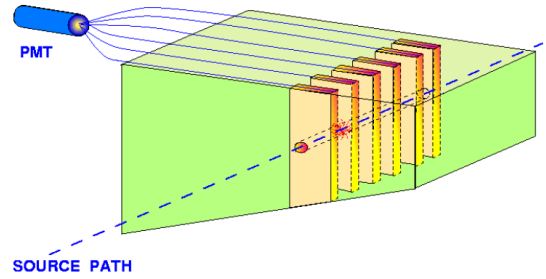

FIG. 2.2: Overall calibration scheme

FIG. 2.3: Flow of ^{137}Cs source during calibration

additional corrections applied to the other layers. The remaining calibration constants are used to correct for both inherent differences and time-varying optical and electrical read-out differences between individual channels. They are calculated using three dedicated calibration systems (cesium, laser, charge injection) that are described in more detail in the following subsections. Each calibration system determines their respective constants to a precision of around 2–3%

2.1. Cesium calibration

The TileCal exploits a radioactive ^{137}Cs source to maintain the global electromagnetic scale and to monitor the optical and electrical response of each PMT in the ATLAS environment. A hydraulic system moves this Cs source through the calorimeter using a network of stainless steel tubes inserted into small holes in each tile scintillator (Figure 2.3). The beta decay of the ^{137}Cs source produces 0.665 MeV photons at a rate of 10^6 Hz, generating scintillation light in each tile. In order to collect a sufficient signal, the electrical read-out of the Cs calibration is performed using the integrator read-out path; therefore the response is a measure of the integrated current in a PMT. The dedicated calibration runs

FIG. 2.1: Calibration chain of TileCal

of the integrator system show that the stability of individual channels was better than 0.05% throughout Run 1.

The high voltage (HV) of each PMT is modified so that the Cs source response in the same PMTs was equal to that observed in the test beam. Corrections are applied to account for differences between these two environments, namely the activity of the different sources and half-life of ^{137}Cs. Three Cs sources are used to calibrate the three physical TileCal partitions in the ATLAS detector, one in the LB and one in each EB. A fourth source is used for beam tests and another is used in a surface research laboratory at CERN.

A full Cs calibration scan through all tiles takes approximately six hours and is performed roughly once per month. The precision of the Cs calibration in one typical cell is approximately 0.3%. For cells on the extreme sides of a partition the precision is 0.5% due to larger uncertainties associated with the source position. Similarly, the precision for the narrow C10 and D4 ITC cells is 3% and 1%, respectively, due to the absence of an iron end-plate between the tile and Cs pipe.

The Cs calibration constants are derived using Cs calibration data taken with the full ATLAS magnetic field system on, as in the nominal physics configuration. The magnetic field effectively increases the light yield in scintillators approximately by 0.7% in the LB and 0.3% in the EB.

Since the response to the Cs source varies across the surface of each tile, additional layer-dependent weights are applied to maintain the electromagnetic scale across the entire calorimeter. These weights reflect the different radial tile sizes in individual layers and the fact that the Cs source passes through tiles at their outer edge.

The total systematic uncertainty in applying the electromagnetic scale from the test beam environment to ATLAS was found to be 0.7%, with the largest contributions from variations in the response to the Cs sources in the presence of a magnetic field (0.5%) and the layer weights (0.3%).

2.2. Laser calibration

A laser calibration system is used to monitor and correct for PMT response variations between Cs scans and to monitor channel timing during periods of collision data-taking.

This laser calibration system consists of a single laser source, located off detector, able to produce short light pulses that are simultaneously distributed by optical fibres to all 9852 PMTs. The intrinsic stability of the laser light was found to be 2%, so to measure the PMT gain variations to a precision of better than 0.5% using the laser source, the response of the PMTs is normalised to the signal measured by a dedicated photodiode. The stability of this photodiode is monitored by an α-source

(^{241}Am) and, throughout 2012, its stability was shown to be 0.1%, and the linearity of the associated electronics response within 0.2%.

The calibration constants, C_{laser}, are calculated for each channel relative to a reference run taken just before a Cs scan, after new Cs calibration constants are extracted and applied. Laser calibration runs are taken for both gains approximately twice per week.

For the E3 and E4 cells, where the Cs calibration is not possible, the reference run is taken as the first laser run before data-taking of the respective year. The total statistical and systematic errors of the laser calibration constants are between 1–2% for the LB and larger for the EBs, where the EBs experience larger current draws due to higher exposure.

2.3. Charge injection calibration

The charge injection system is used to calculate the constant $C_{ADC \rightarrow pC, CIS}$ and applied for physics signals and laser calibration data. A part of this system is also used to calibrate the gain conversion constant for the slow integrator read-out.

All 19704 ADC channels in the fast front-end electronics are calibrated by injecting a known charge from the 3-in-1 cards, repeated for a wide range of charge values (approximately 0–800 pC in low-gain and 0–12 pC in high-gain). A linear fit to the mean reconstructed signal (in ADC counts) yields the constant $C_{ADC \rightarrow pC, CIS}$.

Charge injection calibration data are typically taken twice per week in the absence of colliding beams. For channels where the calibration constant varies by more than 1.0% the constant is updated for the energy reconstruction.

The slow integrator read-out is used to measure the PMT current over 10 ms. Dedicated runs are periodically taken to calculate the integrator gain conversion constant for each of the six gain settings, by fitting the linear relationship between the injected current and measured voltage response. The stability of individual channels is better than 0.05%, the average stability is better than 0.01%.

2.4. Minimum-bias currents

Minimum-bias (MB) inelastic proto–proton interactions at the LHC produce signals in all PMTs, which are used to monitor the variations of the calorimeter response over time using the integrator read-out (as used by the Cs calibration system).[3] The MB rate is proportional to the instantaneous luminosity, and produces signals in all subdetectors, which are uniformly distributed around the interaction point. In the integrator circuit of the Tile Calorimeter this signal is seen as an increased PMT current.

Due to the distribution of upstream material and the

distance of cells from the interaction point the MB signal seen in the TileCal is not expected to be uniform. The largest signal is seen for the A-layer cells which are closer to the interaction point, with cell A13 ($|\eta| = 1.3$) located in the EB and (with minimal upstream material) exhibiting the highest currents.

The currents induced in the PMTs due to MB activity are used to validate response changes observed by the Cs calibration system as well as for response monitoring during the physics runs. Moreover, they probe the response in the E3 and E4 cells, which are not calibrated by Cs.

2.5. Combination of calibration methods

The TileCal response is expected to vary over time, with particular sensitivity to changing LHC luminosity conditions. To disentangle the effects of PMT and scintillator changes one can study the laser versus MB (or Cs) responses.

The PMT gain, as monitored with the laser, is known to decrease with increasing light exposure due to lower secondary emissions from the dynode surfaces.[4] When a PMT is initially exposed to light after a long period of rest, its gain decreases rapidly and then a slow stabilisation occurs. The periods of recovery, where the laser response tends towards initial conditions, coincide with times when LHC is not colliding protons. This is consistent with the known behaviour of fatigued PMTs that gradually return towards original operating condition after the exposure is removed.

The responses to the Cs and MB systems, which are sensitive to both the PMT gain changes and scintillator irradiation show consistent behaviour. The difference between MB (or Cs) and laser response variations is interpreted as an effect of the scintillators irradiation. The transparency of scintillator tiles is reduced after radiation exposure; in the TileCal this is evident in the continued downward response to MB events (and Cs) with increasing integrated luminosity of the collisions, despite the eventual slow recovery of the PMTs as described above. In the absence of the radiation source the annealing process is believed to slowly restore the scintillator material, hence improving the collected light yield. The rate and amount of scintillator damage and recovery are complicated combinations of factors, such as particle energies, temperatures, exposure rates and duration, and are difficult to quantify.

The overlap between the different calibration systems allows calibration and monitoring of the complete hardware and read-out chain of the TileCal, and correct for response changes with fine granularity for effects such as changing luminosity conditions. These methods enable the identification of sources of response variations, and during data-taking, the correction of these variations to maintain the global electromagnetic scale. When possible, problematic components are repaired or replaced during maintenance periods.

3. Study

3.1. Laser study

One third of the laser calibration data taken from 2015 to 2017 is used for these studies. The Laser combined method is used to calculate the corrections. We exclude all channels that are masked. We also exclude those channels flagged as affected for the laser system. Non-instrumented channels are also not used.

i. Study of Laser runs from the year 2015

From Figure 3.1, it can be observed that during the period of data taking, the PMT gain reduces because of an increased dose of radiation (fatigued PMT) and then, it starts recovering in the absence of data taking. Also, since Layer A is closer to the beamline than Layers BC and D, it is more irradiated resulting in larger (absolute) gain drift (This trend can be seen in Figure 3.3 also).

From Figure 3.2, it can be observed that the standard deviation of the PMT gain drift of the layers increases during the period of data taking and reduces when there is no data taking. This can be attributed to the fact that during data taking, the reduction in PMT gain (which is due to the reduction of secondary emissions from PMT dynode), which is a random process, shows a larger spread with increased radiation dosage.

From Figure 3.3, one can observe the variation of PMT gain drift along the beam axis for three layers. Due to distribution of the upstream material and distance of cells from the interaction point, the gain drift seen in TileCal is not uniform. The largest drift is seen for layer A cells which are closest to the interaction point, A13 located in the EB (with minimum upstream material) exhibits the maximum drift. Layer BC and D show smaller gain drift. In Figure 3.4, the cells with large RMS values are due to some outliers, channels with large drifts that should be investigated.

From Figure 3.5–3.8, it can be observed that both, the (absolute value) mean and the standard deviation are larger for extended barrel in comparison to those for long barrel (for a particular layer), which is due to the higher irradiation of the cells in the extended barrel than those in long barrel. From these distributions, one can again draw the same conclusions about the difference in drift for the three layers. If Figure 3.5 (3.6) is compared with Figure 3.7 (3.8), same observations about the increase in mean and spread of the distribution can be made out due to the process of data taking.

In the laser calibration, a total of 384 fibres distribute the laser light into the TileCal PMTs. An additional splitting of the light is performed at the level of each module to distribute the light on each PMT. Each ex-

tended barrel module (EBA and EBC) is fed by two fibres (16 PMTs per fibre) and each long barrel module (two partitions LBA and LBC) is fed by two fibres (45 PMTs per fibre). So each cell being measured by two PMTs (which experience almost same irradiation) provides a more accurate result in laser calibration constant. This redundancy also helps in the cases when one PMT is lost (dead).
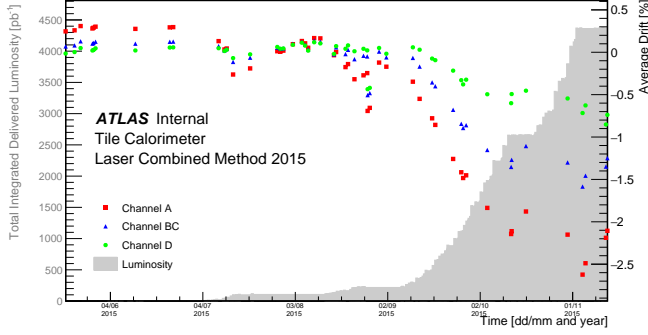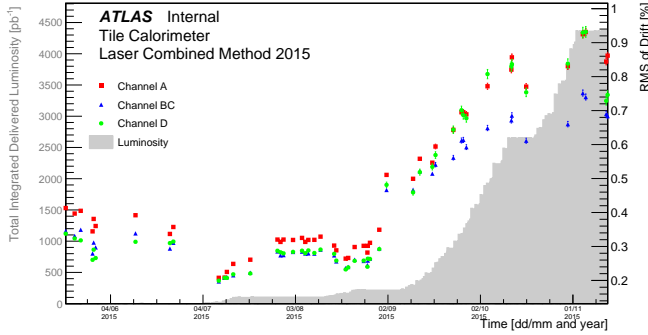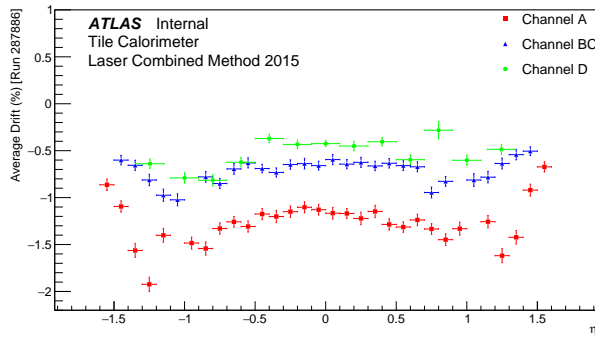
be explained on the same basis as for Figure 3.2. The distributions for ΔPMT (Figure 3.11–3.14) show exactly same trend as observed for the distributions for PMT gain drift (Figure 3.5–3.8).

FIG. 3.1: Average Drift vs Time

FIG. 3.4: RMS of Drift vs η (Dec 12, 2015)

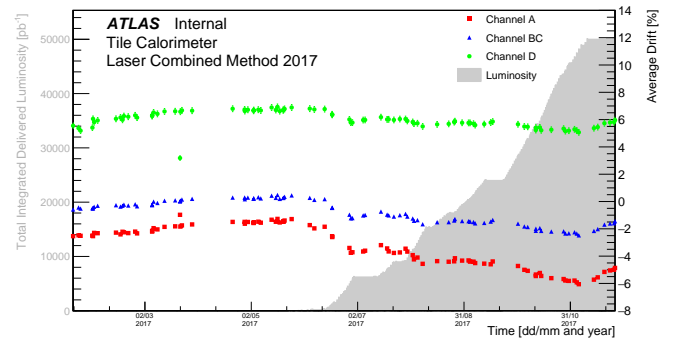FIG. 3.2: RMS of Drift vs Time

FIG. 3.5: Distribution of Drift (May 20, 2015) (Long Barrel)

FIG. 3.3: Average Drift vs η (Dec 12, 2015)

From Figue 3.9, it can be observed that the mean of ΔPMT is around zero. The trend of the Figure 3.10 can
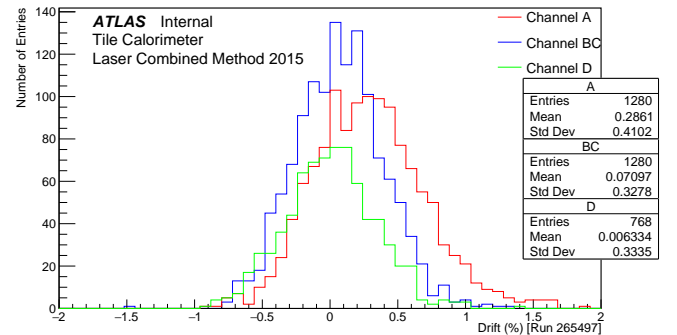
FIG. 3.6: Distribution of Drift (May 20, 2015) (Extended Barrel)
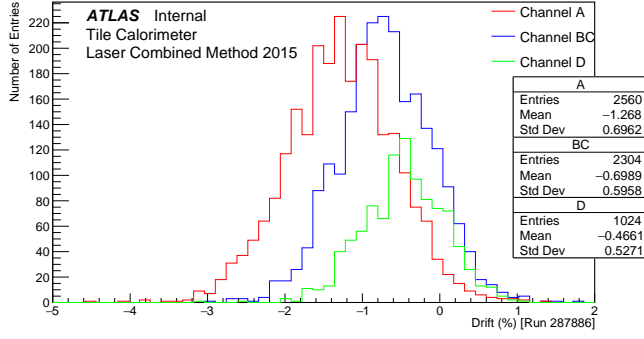
FIG. 3.7: Distribution of Drift (Dec 12, 2015)
(Long Barrel)
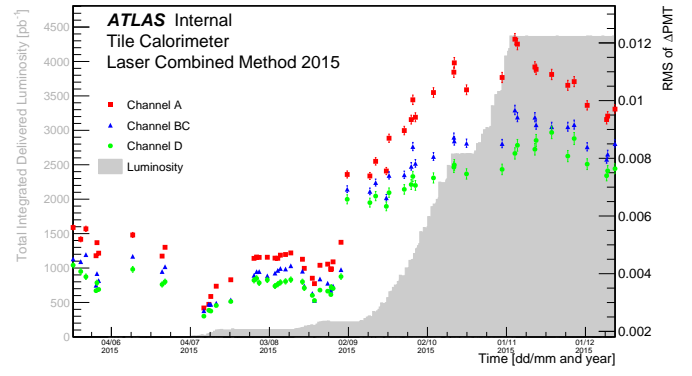
FIG. 3.10: RMS of ΔPMT vs Time
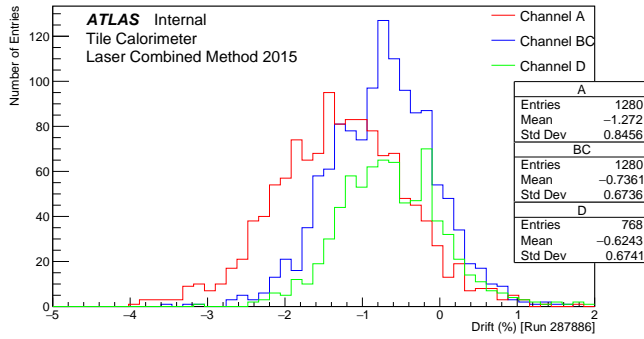
FIG. 3.8: Distribution of Drift (Dec 12, 2015)
(Extended Barrel)
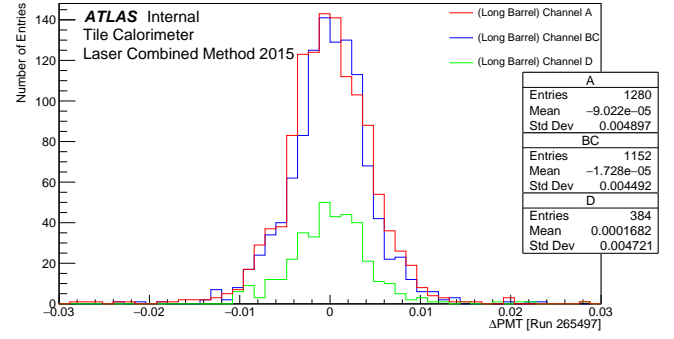
FIG. 3.11: Distribution of ΔPMT (May 20, 2015)
(Long Barrel)
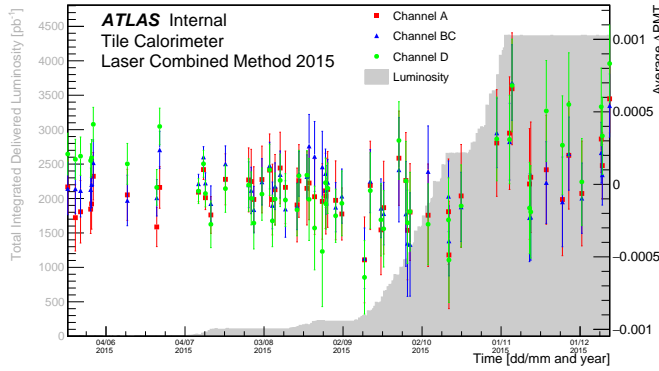
FIG. 3.9: ΔPMT vs Time
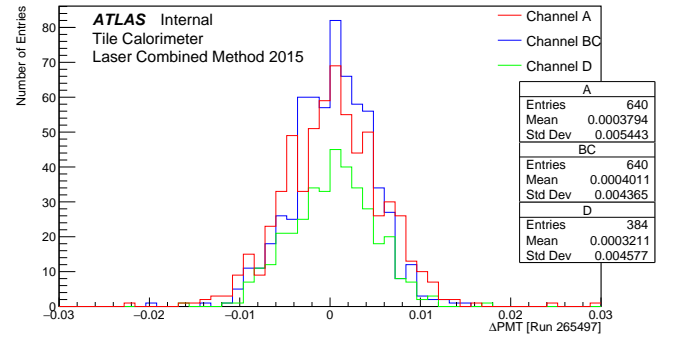
FIG. 3.12: Distribution of ΔPMT (May 20, 2015)
(Extended Barrel)
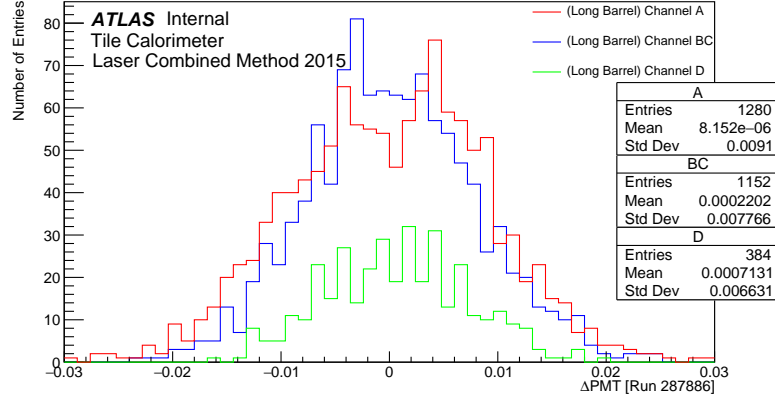
FIG. 3.13: Distribution of ΔPMT (Dec 12, 2015)
(Long Barrel)
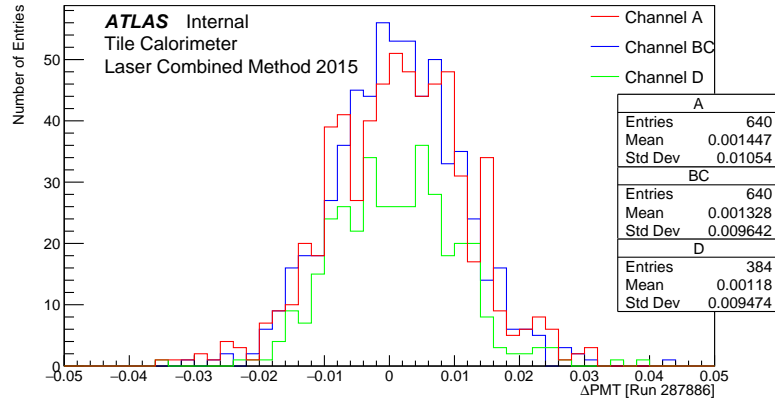
FIG. 3.14: Distribution of ΔPMT (Dec 12, 2015)
(Extended Barrel)

ii. Study of Laser runs from the year 2016

From Figure 3.15 (3.16), it can be observed that there is a jump in Average (RMS) of PMT gain drift around April 2016, which is because of the increase in High Voltage (HV) for the PMTs for D5 and D6 cell. This jump can be removed if the laser reference run is taken just after the increase in HV. Apart from this, all the plots of the year 2016 show the same trend as shown by plots of the year 2015.
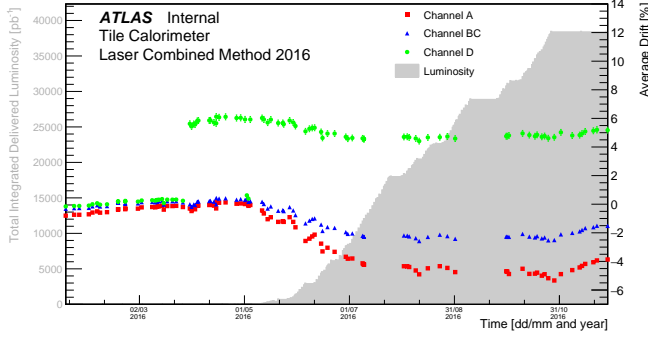
FIG. 3.15: Average Drift vs Time
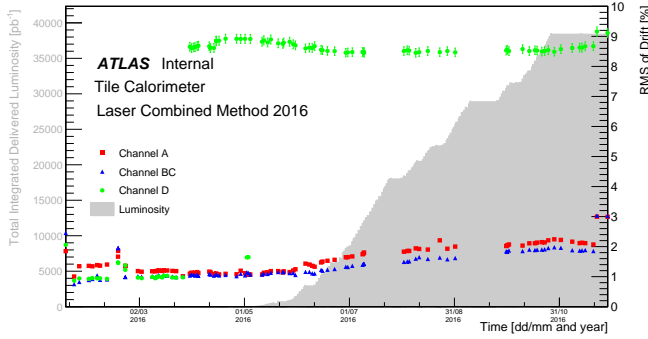
FIG. 3.16: RMS of Drift vs Time
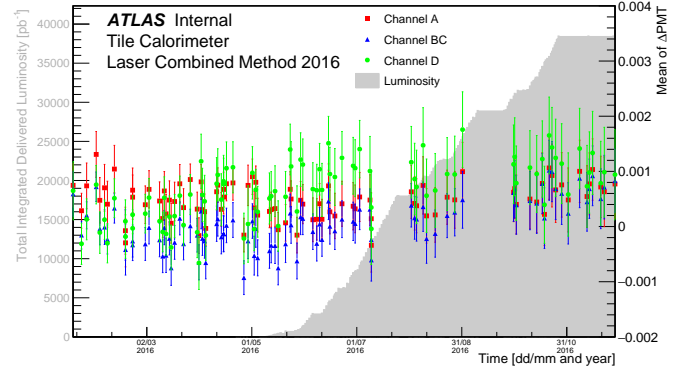
FIG. 3.17: ΔPMT vs Time
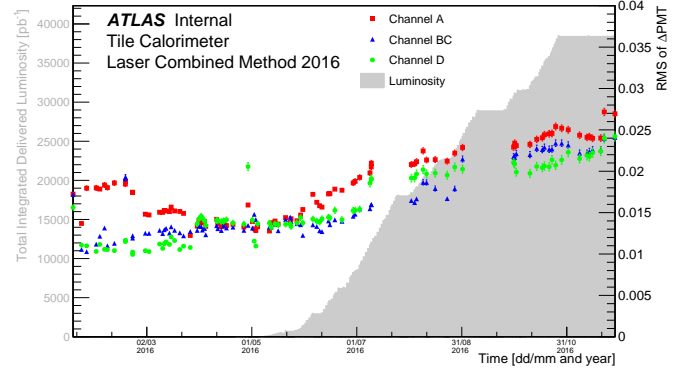
FIG. 3.18: RMS of ΔPMT vs Time

iii. Study of Laser runs from the year 2017

The same jump and a similar trend is observed for the plots for the year 2017.

FIG. 3.19: Average Drift vs Time
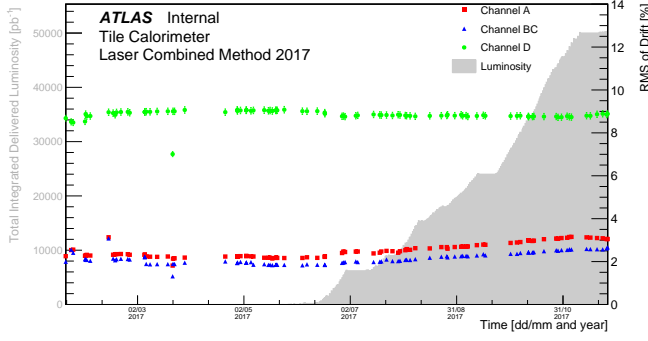
FIG. 3.20: RMS of Drift vs Time
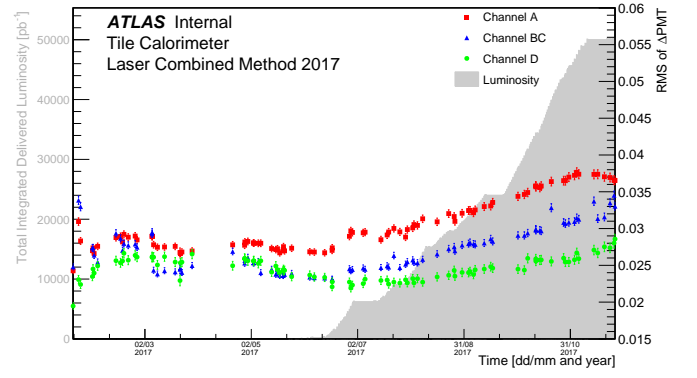
FIG. 3.22: RMS of ΔPMT vs Time
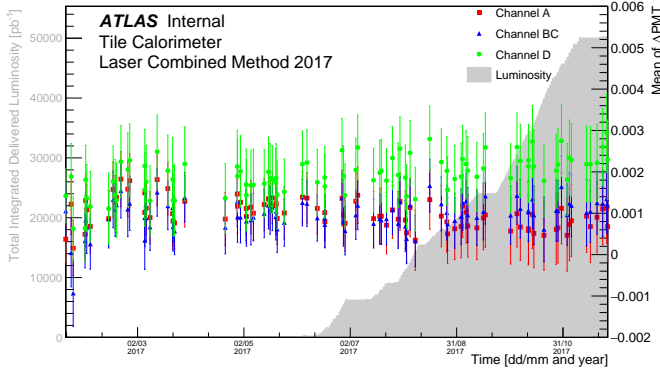
FIG. 3.21: ΔPMT vs Time
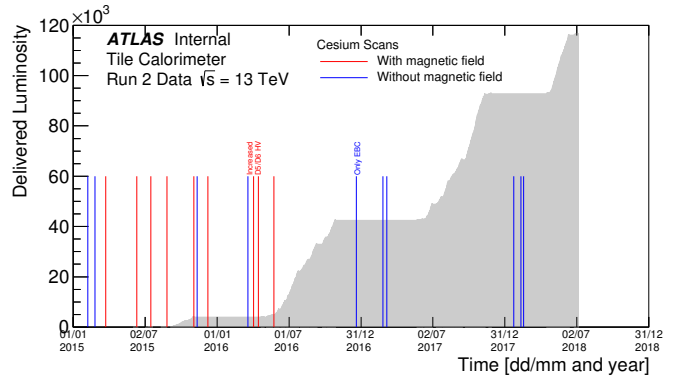
FIG. 3.23: Cesium scans in Run 2

3.2. Study of comparison between Cesium and Laser calibration

The drifts measured by Cesium and Laser system during several time periods (IOV), according to Cesium scan availability, are compared. Comparison is started for the year 2015, where more scans were performed and 2 IOVs are defined, covering different data taking periods. Laser runs are selected within one day of the Cesium scan. Cesium data are extracted from Cesium constants from COOL Database. Different IOVs taken for analysis:

- CESIUM (from DB, all with magnetic field)
  IOV1: 263962 (11/june) ↔ 270000 (17/july)
  IOV2: 270000 (17/july) ↔ 284600 (3/nov)

- LASER (new combined method)
  IOV1: 267534 (12/june) ↔ 272493 (19/july)
  IOV2: 272493 (19/july) ↔ 284682 (4/nov before Cs)
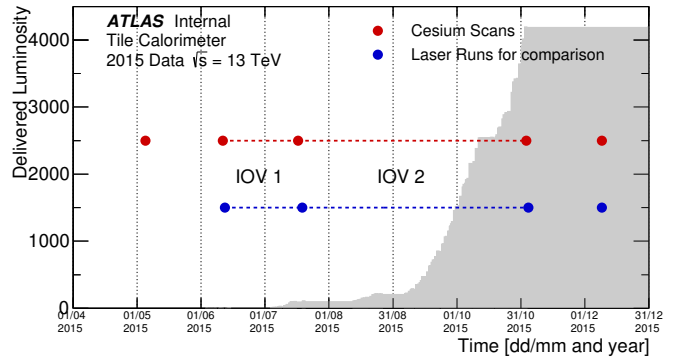
FIG. 3.24: IOVs taken for analysis

i. 2D Plots

For Figures 3.25–3.28, the points near the origin are channels which are seen as stable by the cesium and the laser systems. In the diagonal, these are channels which are seen as drifting by both calibration systems. A difference between the laser and the cesium calibration constants can, in principle, come from a read-out electronics

issue (the signal produced during the laser or the cesium calibration runs is not treated by the same electronics), a scintillator ageing effect, bad cesium calibration for a few channels.

For IOV1 (Figure 3.25, 3.27) when there is less data taking, the distribution is around the line y=x (black line) and the distribution for different layers are well overlapping (Figure 3.27). For IOV2 (Figure 3.26, 3.28) when the data taking increases, the distribution shifts below the black line. Also the distribution for each layer (Figure 3.28) are well seperated because of the difference in their irradiation.
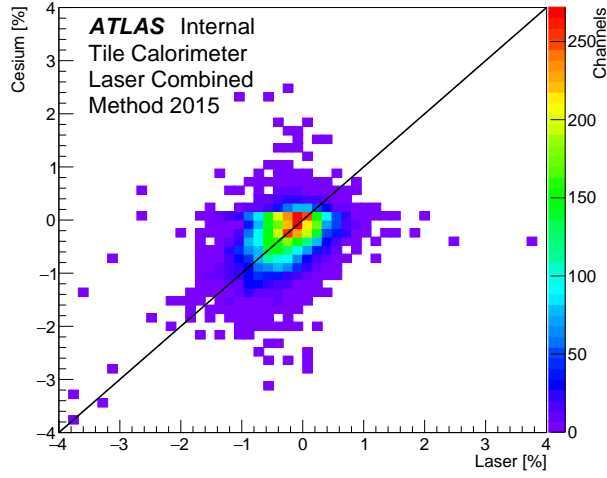
FIG. 3.25: Cesium vs Laser drift for all instrumented channels
(IOV1)
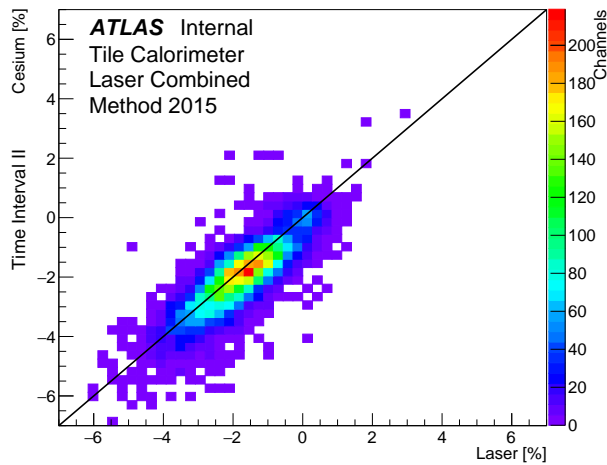
FIG. 3.26: Cesium vs Laser drift for all instrumented channels
(IOV2)
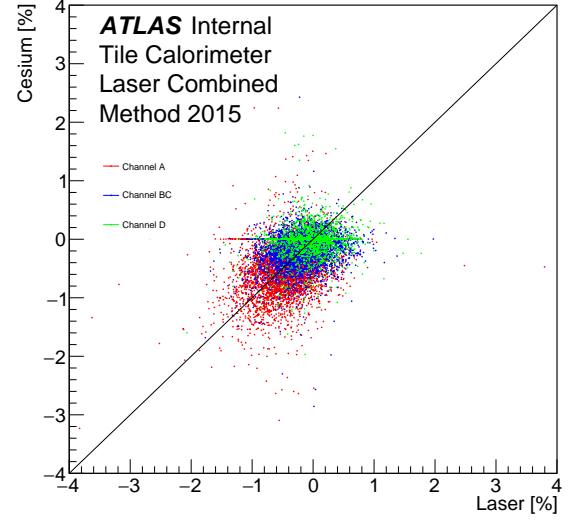
FIG. 3.27: Cesium vs Laser drift for different channels
(IOV1)
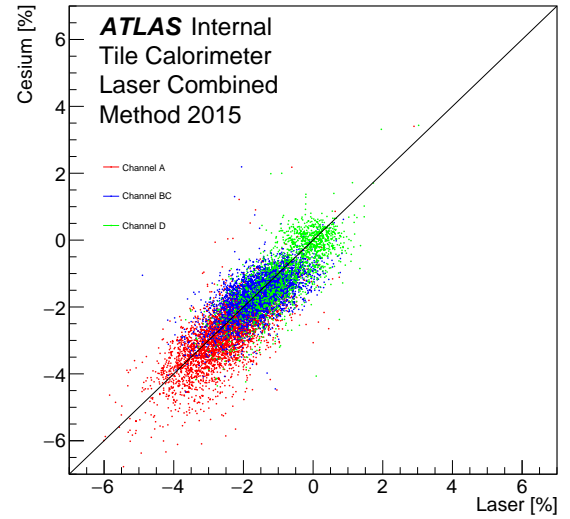
FIG. 3.28: Cesium vs Laser drift for different channels
(IOV2)

ii. 1D Plots

From Figure 3.29 and 3.32, it can be observed that the spread and mean in laser as well as cesium drift increases on going from long barrel to extended barrel for Layer A. The same observation can be made for different layers for a particular IOV. The unusual peak at zero (Figure 3.30, 3.32, 3.34) for Cesium response in IOV1 means that there are many cells in the extended barrel showing very less (but not exactly zero) Cs response drift. The cells are still under investigation.

For IOV2 (Figure 3.35–3.40), it can be observed that the cesium calibration shows a larger (absolute) drift than that shown by laser calibration.
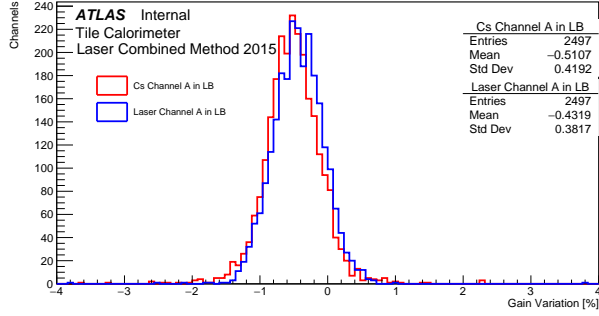

FIG. 3.29: Distribution of Laser and Cesium drift for layer A
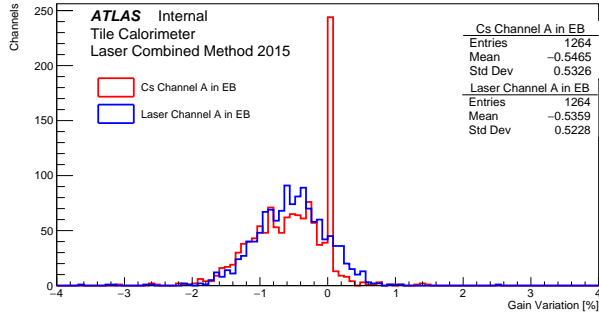Long barrel (IOV1)

FIG. 3.30: Distribution of Laser and Cesium drift for layer A
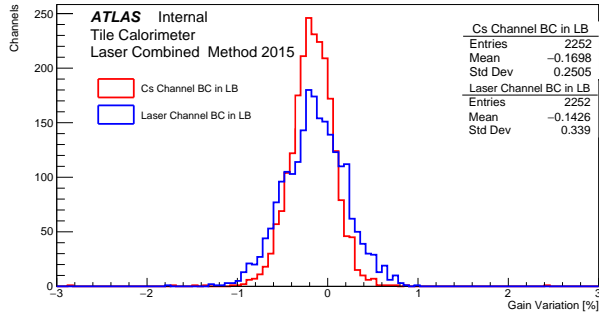Extended barrel (IOV1)

FIG. 3.31: Distribution of Laser and Cesium drift for layer BC
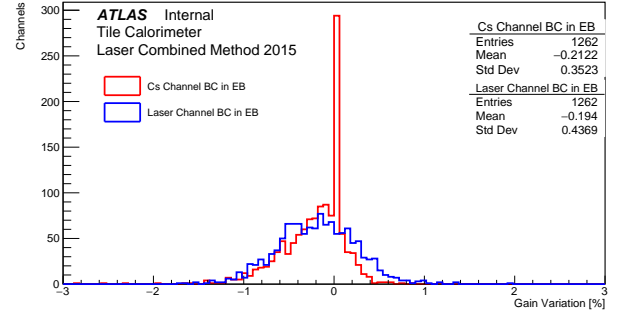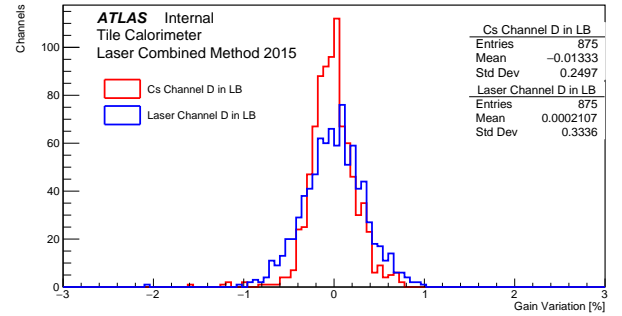Long barrel (IOV1)

FIG. 3.32: Distribution of Laser and Cesium drift for layer BC
Extended barrel (IOV1)

FIG. 3.33: Distribution of Laser and Cesium drift for layer D
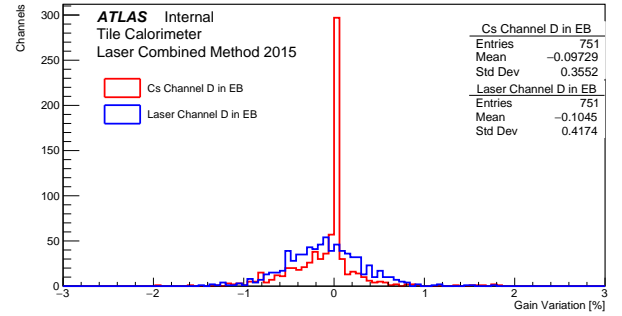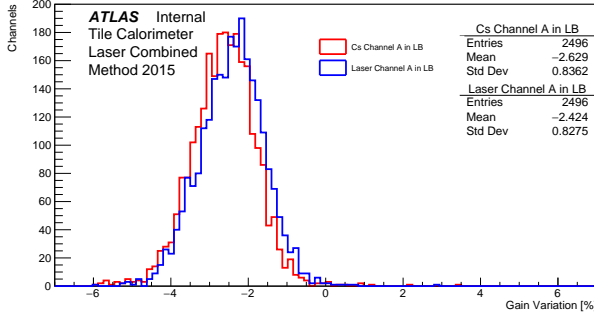Long barrel (IOV1)

FIG. 3.34: Distribution of Laser and Cesium drift for layer D
Extended barrel (IOV1)

FIG. 3.35: Distribution of Laser and Cesium drift for
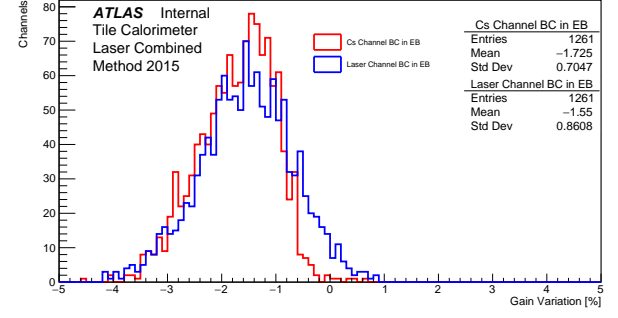layer A
Long barrel (IOV2)

FIG. 3.38: Distribution of Laser and Cesium drift for
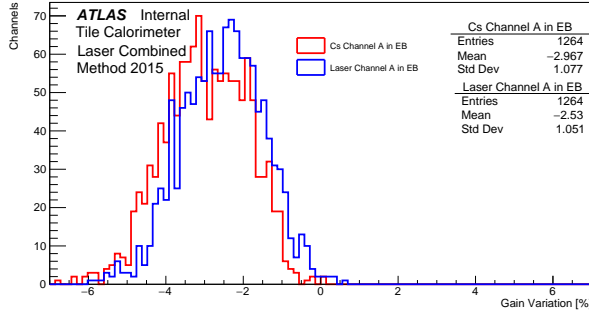layer BC
Extended barrel (IOV2)

FIG. 3.36: Distribution of Laser and Cesium drift for
layer A
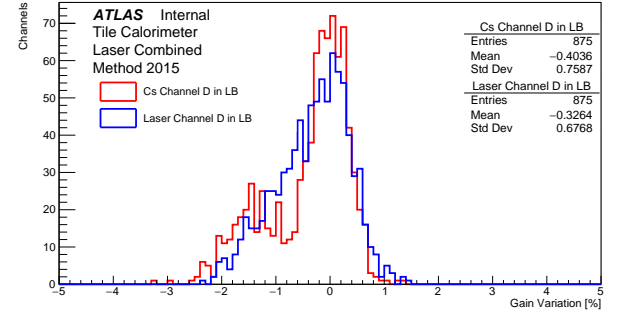Extended barrel (IOV2)

FIG. 3.39: Distribution of Laser and Cesium drift for
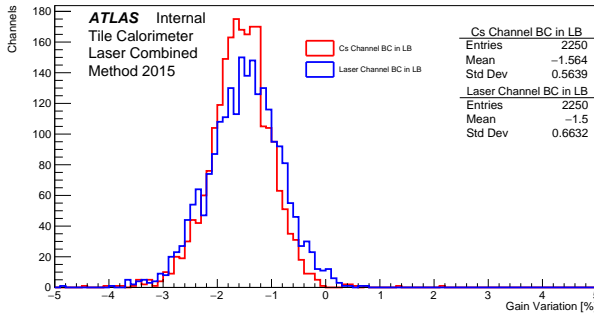layer D
Long barrel (IOV2)

FIG. 3.37: Distribution of Laser and Cesium drift for
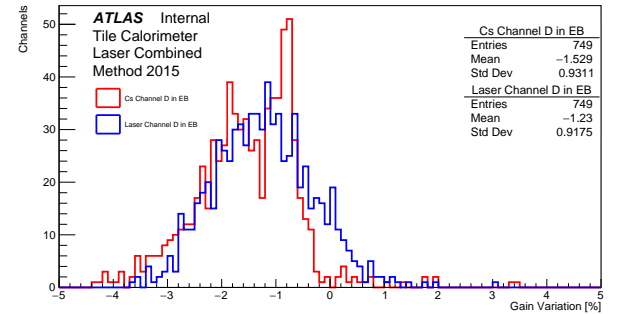layer BC
Long barrel (IOV2)

FIG. 3.40: Distribution of Laser and Cesium drift for
layer D
Extended barrel (IOV2)

iii.   1D plots for f_{las}/f_{Cs}

For each pair of laser run/cesium scan, the ratio of laser calibration constants and cesium calibration constants is considered.

$$f = \frac{1}{1 + \Delta_{drift}} \qquad (2)$$

Equation-2 defines f, which is the calibration constant and Δ_{drift} is the drift measured in a given time interval. Pathological channels (masked and non-instrumented) are not considered in the comparisons. The distribution is fitted to a Gaussian function. The mean obtained by the fit quantifies the compatibility of the two calibration systems and is interpreted as the systematics on the laser calibration constants. The σ obtained by the fit can be interpreted as a measure of the systematic uncertainty of the laser system measurement, assuming that the uncertainty on the cesium calibration constants is negligible with respect to the laser one.

A difference between the laser and the cesium calibration constants can, in principle, come from a read-out electronics issue (the signal produced during the laser or the cesium calibration runs is not treated by the same electronics), a scintillator ageing effect, bad cesium calibration for a few channels.

TABLE I: Spread of the ratio f_{Las}/f_{Cs}, obtained by a Gaussian fit

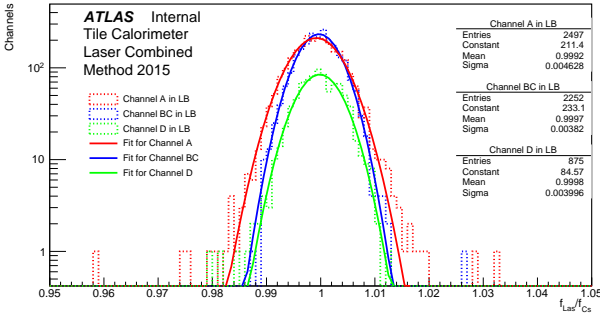| Period IOV	Barrel	Range of fit-width (%) σ
1	Long barrel	0.3–0.4
1	Extended barrel	0.5–0.6
2	Long barrel	0.5–0.6
2	Extended barrel	0.6–0.7

FIG. 3.41: Distribution of Laser/Cesium constant for different layers
Long barrel (IOV1)

The Gaussian-fitted mean values tell about the extent of agreement between the laser and cesium measurement, and if they disagree, then a potential bias of the laser measurement can be learnt about.
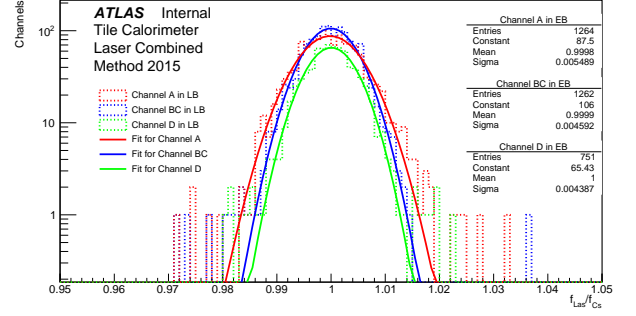

FIG. 3.42: Distribution of Laser/Cesium constant for different layers
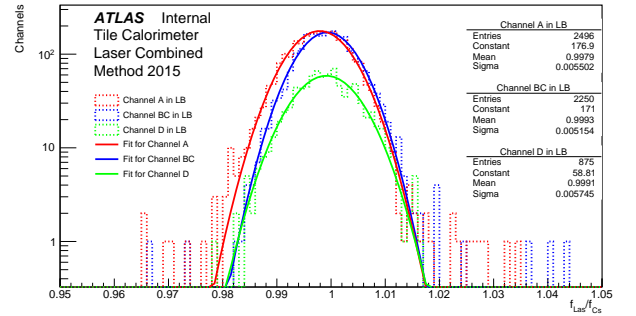Extended barrel (IOV1)

FIG. 3.43: Distribution of Laser/Cesium constant for different layers
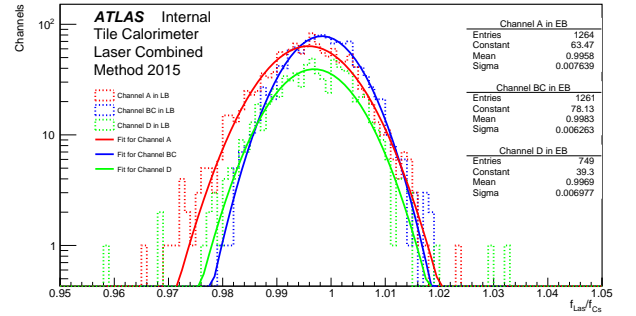Long barrel (IOV2)

FIG. 3.44: Distribution of Laser/Cesium constant for different layers
Extended barrel (IOV2)

From the figures (Figure 3.41–3.44) and Table 1, it can be observed that the width of the fit increases from Long barrel to Extended barrel. The width of the fit (for a particular barrel) increases from IOV1 to IOV2, due to data taking of $\sim 4fb^{-1}$ (Figure 3.24, 3.45) from IOV1 to IOV2.
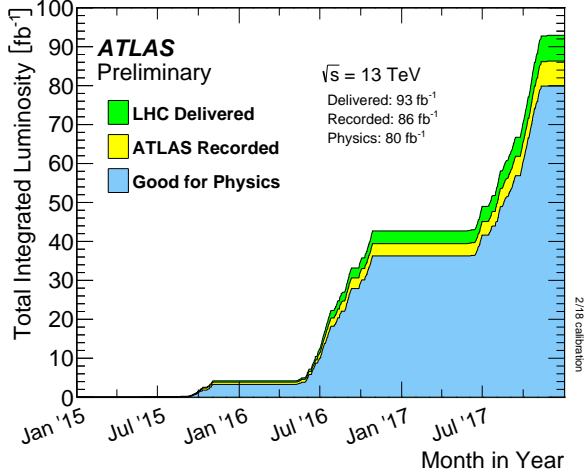

FIG. 3.45: Luminosity vs Time (Run2)

4.   Conclusion and Future Works

- This study will continue to include a comparison of Cesium–Laser for 2016 and 2017 (covering the full year).

- Due to the larger amount of delivered luminosities in these years (Figure 3.45), larger drifts in the response are expected.

- For the last years, a deviation between the laser and cesium response drift measurements for some of the more irradiated cells is expected. This can be attributed to the scintillator ageing.

- The ultimate goal of this paper and future work is to extract conclusions from the comparison with Cesium measurements and approve some of the included plots for public use.

5.   References

- ATLAS Collaboration, *The ATLAS Experiment at the CERN Large Hadron Collider,* JINST 3 (2008) S08003

- ATLAS Collaboration, *ATLAS tile calorimeter: Technical Design Report,* 1996, URL: http://cds.cern.ch/record/331062.

- ATLAS Collaboration, *Operation and performance of the ATLAS Tile Calorimeter in Run 1 (2018),* arXiv:1806.02129

- ATLAS Collaboration, *The Laser calibration of the ATLAS Tile Calorimeter during the LHC run 1,* J. Abdallah et al JINST 11 (2016) T10005

[1] ATLAS uses a right-handed coordinate system with its origin at the nominal interaction point (IP) in the centre of the detector and the z-axis along the beam pipe. The x-axis points from the IP to the centre of the LHC ring, and the y-axis points upward. Cylindrical coordinates (r, ϕ) are used in the transverse plane, ϕ being the azimuth angle around the z-axis. The pseudorapidity is defined in terms of the polar angle θ as $\eta = -ln(tan(\theta/2))$.

[2] The corresponding calibration constant converts the calorimeter signals, measured as electric charge in pC, to energy deposited by electrons that would produce these signals.

[3] The usage of the integrators allows for a high rate of minimum-bias events, much higher than could be achieved with the fast read-out.

[4] The decrease in the gain depends on several factors, including temperature, intensity and duration of the light exposure, and previous history of the PMT.